Experimental investigation into the impact of a liquid droplet onto a granular bed using three-dimensional, time-resolved, particle tracking

Edward J. Long,[1] Graham K. Hargrave,[1] James R. Cooper,[2] Ben G. B. Kitchener,[3] Anthony J. Parsons,[3] Caspar J. M. Hewett,[4] and John Wainwright[4]

[1]*Wolfson School of Mechanical and Manufacturing Engineering, Loughborough University, Leicestershire, United Kingdom*
[2]*School of Environmental Sciences, University of Liverpool, Liverpool, United Kingdom*
[3]*Department of Geography, University of Sheffield, Sheffield, United Kingdom*
[4]*Department of Geography, Durham University, Durham, United Kingdom*

(Received 10 June 2013; published 3 March 2014)

An experimental investigation into the interaction that occurs between an impacting water droplet and a granular bed of loose graded sand has been carried out. High-speed imaging, three-dimensional time-resolved particle tracking, and photogrammetric surface profiling have been used to examine individual impact events. The focus of the study is the quantification and trajectory analysis of the particles ejected from the sand bed, along with measurement of the change in bed morphology. The results from the experiments have detailed two distinct mechanisms of particle ejection: the ejection of water-encapsulated particles from the edge of the wetted region and the ejection of dry sand from the periphery of the impact crater. That the process occurs by these two distinct mechanisms has hitherto been unobserved. Presented in the paper are distributions of the particle ejection velocities, angles, and transport distances for both mechanisms. The ejected water-encapsulated particles, which are few in number, are characterized by low ejection angles and high ejection velocities, leading to large transport distances; the ejected dry particles, which are much greater in number, are characterized by high ejection angles and low velocities, leading to lower transport distances. From the particle ejection data, the momentum of the individual ballistic sand particles has been calculated; it was found that only 2% of the water-droplet momentum at impact is transferred to the ballistic sand particles. In addition to the particle tracking, surface profiling of the granular bed postimpact has provided detailed information on its morphology; these data have demonstrated the consistent nature of the craters produced by the impact and suggest that particle agglomerations released from their edges make up about twice the number of particles involved in ballistic ejection. It is estimated that, overall, about 4% of the water-droplet momentum is taken up in particle movement.

DOI: 10.1103/PhysRevE.89.032201 PACS number(s): 45.70.−n, 45.50.−j

I. INTRODUCTION

The impact of a liquid droplet onto a bed of granular media is a highly complex interaction in which the mechanisms of energy transfer are difficult to quantify. Even considering the simplified case of a solid projectile, granular systems have been shown to exhibit particularly abstruse rheology, demonstrating both solidlike and liquidlike responses to external impact [1,2]. Many studies have investigated this complex response of granular media to solid impact, looking at both bed morphology [2–4] and the ejection of particles [5,6], considerably adding to our understanding. However, such studies provide limited insight into the additional complexities provided by a liquid projectile, in which deformation and breakup of the droplet, in conjunction with its penetration into the granular medium, has considerable influence on the transfer of energy. The case of a droplet hitting a granular medium has been well documented for the specific case of rain-splash transport in soil-erosion studies, with several papers looking at the process of grain transport [7–9] as well as crater formation [10]. Even though this process of splash transport has received considerable attention, little is known about the transfer of momentum between droplets and granular media [9], with only a few recent studies investigating the fundamental interactions involved [9,11–13]. The aim of the work presented in this paper is to provide further insight into this complex interaction between a droplet and a granular medium and derive the momentum transfer that occurs during an impact event. To this end, the movement of the particles ejected from a sand bed during a droplet impact has been recorded and analyzed for four separate events, enabling the momentum transfer from the water to the ejected sand to be calculated.

The nature of the interaction that occurs between the water and the sand is controlled by a large number of variables such as droplet size, impact velocity, fluid viscosity, surface tension, grain size, grain shape, and packing density. However, for this study, all of these variables were kept constant, with four runs made of the same individual interaction, in order to examine the complexities of the event. To investigate the interaction that occurs, three techniques were used: (i) high-speed imaging of the impact, looking at the movement of both the water and the sand, so that the development of the interaction can be understood; (ii) three-dimensional, time-resolved, particle tracking of the ejected sand grains, so that particle ejection velocity, angle, and total transport distance can be measured; and (iii) surface profiling of the impact crater and the large clumps of sand transported from the crater edge, so that the change in bed morphology produced by the impact can be examined.

II. THE EXPERIMENTS

The experiments carried out in this study consisted of a 3.6-mm-diameter droplet of water impacting on a bed of

graded sand which had a grain size ranging from 150 to 160 μm. This droplet size was selected as it is typical of the size found in high-intensity, erosive rainfall [14]. The droplet was formed by displacing water through a blunt-ended tube, 0.8 mm in external diameter, using a stepper motor-driven plunger; the rotational speed and distance of the motor was controlled in order to produce repeatable drop formation. The water droplet detached from the tube tip and fell under gravity through a distance of 3 m onto the sand bed, reaching a velocity of 6.45 m s^{-1} before impact. High-velocity impact (within the limit of terminal velocity) is of specific interest when investigating droplet impact due to the high level of energy available for bed deformation and material transport. Terminal velocity for this size of droplet is 8.6 m s^{-1} [15]; a velocity unavailable at the time of testing due to height restrictions. The droplet fell through a 35-mm internal-diameter tube for the majority of its descent in order to prevent any local air movement from causing lateral drop movement. The sand particles were held within a container with internal dimensions of 160 by 160 by 15 mm, placed upon a leveled surface. The sand was dried and poured into the container without compaction, the excess being scraped from the surface by a straight edge to produce a flat, level surface prior to impact. This process produced a packing density (ϕ) of 0.50. A light gate was positioned below the droplet-generation tube in order to trigger the recording equipment after the droplet was released.

III. DROPLET IMPACT IMAGING

To gain insight into the process of a liquid droplet impacting upon a granular bed, high-speed imaging was carried out. Three different imaging techniques were utilized in this study: (i) whole-field imaging, in which the impact region is illuminated so that the sand bed, water droplet, and ejecta were all visible; (ii) fluorescence imaging, in which fluorescent dye was added to water so that, with the use of filters, only the water was visible in the images; and (iii) ejecta imaging, in which the illuminating light was directed parallel to the bed so that, after some image processing, only particles ejected from the bed surface were visible.

A. Whole-field imaging

Whole-field imaging of the impact event is shown in Fig. 1. The images were acquired using a Photron APX-RS camera, running at 10 000 frames per second with a resolution of 512 by 512 pixels, fitted with a 105-mm macro lens. The camera was mounted to look down on the impact region at an angle of 50° to the sand bed, providing a view of both the crater formation and the ejected material. The image region was approximately 23 by 30 mm in size. Illumination was provided by a fiber-coupled copper-vapor laser synchronized to the camera frame rate. The light was directed onto the bed from a position slightly below and to the left of the camera. In Fig. 2 every 20th image recorded is presented (providing a

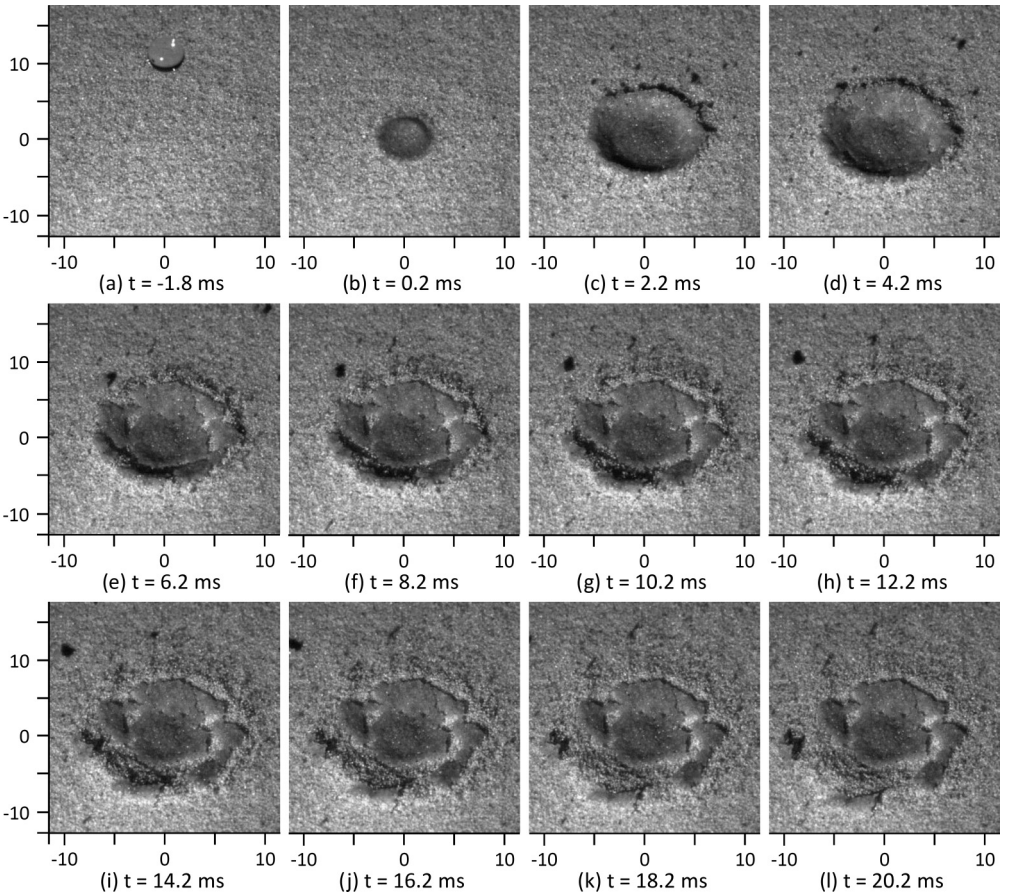

FIG. 1. Image sequence of a 4-mm water droplet hitting a granular bed of 150–160-μm-diameter sand particles at a velocity of 6.5 m s^{-1}.

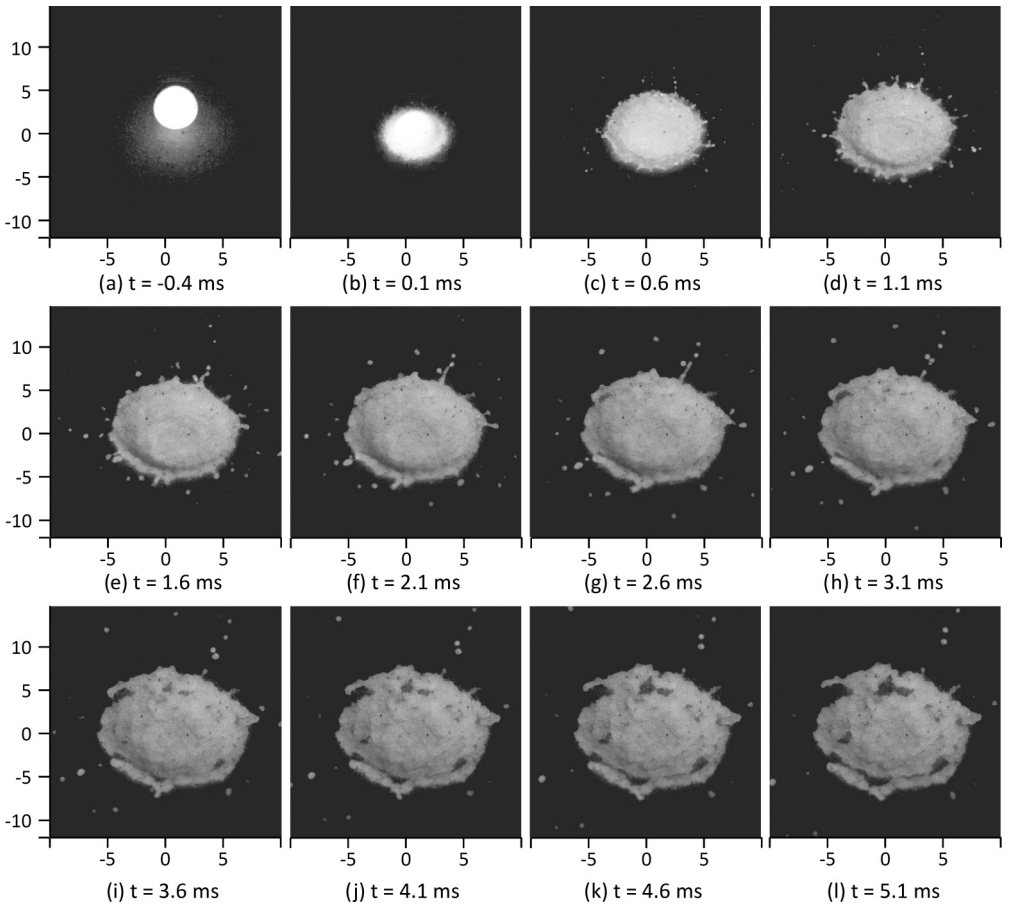

FIG. 2. Fluorescence imaging of a 4-mm water droplet hitting a granular bed of 150–160-μm-diameter sand particles at a velocity of 6.5 m s^{-1}.

2-ms interval between frames) so that sufficient development of the interaction can be shown; only images from the first ~20 ms are displayed, it takes ~85 ms for all movement to finish.

Figure 1 shows the droplet hitting the granular bed and deforming on impact [panel (b)]. It is apparent that rapid penetration of the liquid into the granular layer occurs, displacing the air between the grains and forming a slurry of sand and water [panel (c)], referred to by Furbish *et al.* [9] as a "mat" of wetted grains. As the water impacts and penetrates, the granular bed itself is deformed as momentum is transferred from the liquid to the sand, creating a shallow crater in the surface. The crater formed in the sand bed rapidly increases in radial diameter during the early stages of the interaction [panels (b) to (e)] as the water, unable to make further progression through the sand bed, undergoes momentum transfer from vertical to lateral movement. During the radial expansion of the crater, ejecta from the edge of the sand-water mixture lining the crater are released, a process that can be seen to start in panel (c).

These ejecta have a high velocity (greater than 2 m s^{-1}), moving rapidly through the image region; they are looked at in more detail in Sec. III B. As the radial diameter of the crater continues to grow and penetration of the water continues, a point is reached at which the mixture of sand and water has insufficient liquid to encapsulate any more grains fully, given the surface tension of the liquid. Therefore, as expansion of the crater continues and the encapsulated grains move further apart, the surface tension of the water holding the grains together is overcome. As a result, the mat of wetted sand starts to break up into sections, revealing dry sand through the cracks. These cracks therefore appear as lighter areas between the darker wet regions [panel (e) onwards]. Part of this breakup process results in a few small agglomerations of wet sand leaving the edge of the crater, some acting like large projectiles, others bouncing or rolling away from the lip. In addition to movement of sand grains that come into direct contact with the liquid, there is an ejection of dry sand grains from the periphery of the mat of wetted grains, although they are difficult to identify from the still images of Fig. 1. These particles are first noticeable in panel (e) and appear to originate from under the water-penetrated layer, displaced by the downward pressure of the droplet impact and the resistance of the lower bed to vertical movement. This ejection of particles is examined in more detail in Sec. III C.

B. Fluorescence imaging

Fluorescence imaging of the impact event is shown in Fig. 2. This technique was employed in order to visualize the movement, penetration and breakup of the water during the impact event. In order to show only the water movement, a

small quantity of rhodamine 640 perchlorate was mixed with the droplet water so that the water fluoresced at a wavelength substantially above the incidental light. A long-pass filter was then positioned in front of the camera lens so that only the light from the fluorescing water could pass through to the camera, rejecting the light scattered from the sand. A copper-vapor laser, producing light at 510.6 and 578.2 nm, was used as the illumination source, resulting in the water fluorescing in the 605–633-nm range. The images were acquired using a Photron APX-RS camera, running at 10 000 frames per second with a resolution of 512 by 512 pixels, fitted with a 105-mm macro lens. The camera was mounted at the same angle as the whole-field imaging (50° to the bed), but the image region size was reduced to approximately 20 by 26 mm. In Fig. 2 every fifth image recoded is presented (providing a 0.5-ms interval between frames) so that sufficient development of the water movement could be shown; only images from the first ∼5 ms are displayed.

From the image sequence shown in Fig. 2, the deformation and rapid penetration of the droplet can be clearly seen. By Fig. 2(d), a time span of just 1.1 ms from impact, the droplet has penetrated into the sand, revealing the texture of the granular material without a smooth liquid layer sitting above it. During this initial stage of the impact, splash droplets are ejected from the impact region [Figs. 2(b) and 2(c)] that are smaller than the grain size of the bed, demonstrating their composition to be entirely liquid. As the interaction continues, and the wetted region expands radially, the edge of the water-sand mixture starts to "finger" in a similar manner to that found with liquid hitting a solid surface and producing a splash crown [16]. The fingering process of the water-sand slurry is considerably less pronounced than that of pure liquid, with the finger ligaments rapidly breaking up into discrete ejecta. The sizes of the ejecta produced vary from slightly larger than an individual sand grain up to around three sand grains in diameter; the nonspherical shape of some of them indicating a composition of both sand and water. The breakup of the wetted sand mat, seen in Fig. 2(f) onwards, shows that the periphery of the wetted region is only a few grains of sand deep and water has not penetrated beyond this point.

C. Ejecta imaging

Imaging of ejecta from the droplet impact is shown in Fig. 3. For this imaging technique, the illumination was provided by multiple pulsed LEDs positioned around the impact event. Each LED was fitted with a focusing lens and oriented so that the light was projected horizontal to the sand bed; an arrangement which resulted in strong illumination of the ejecta but minimal illumination of the bed surface. Postprocessing of the image sequence was carried out by comparing each frame to an image of the bed before the droplet impact, thus removing any illumination of the static sand bed. The images were acquired using a Photron SA3 camera, running at 2000 frames per second, with a resolution of 1024 by 1024 pixels fitted with a 105-mm macro lens. The camera was mounted to look down on the impact region at an angle of 60° to the sand bed and the image region size was approximately 60 by 64 mm. In Fig. 3 every sixth image recoded is presented (providing a 3-ms interval between frames) so that sufficient development of the ejection process can be shown; only images from the first ∼40 ms are displayed.

The ejecta-imaging technique reveals the release of projectiles from the impact event with greater clarity than either the whole-field imaging or the fluorescence-imaging techniques. With this approach, the three main forms of particle release are visible: the early release of ejecta from the edge of the wetted sand mat [Fig. 3(b)], the dry discrete sand particles from the periphery of the crater [Fig. 3(d) onwards], and the movement of particle agglomerations breaking off from the wetted region [Fig. 3(f) onwards]. The release of the small water droplets, recorded in the fluorescence imaging, can be seen faintly in Fig. 3(b) towards the top of the image. The water-sand ejecta, released from the edge of the wetted region, move rapidly through the image area from Fig. 3(b) onwards and move outside the recorded region before coming to rest; however, there are relatively few ejecta involved in this form of release. In contrast, the dry particles released by the impact [Fig. 3(d) onwards] do not appear to travel very far, the majority coming to rest within the 30-mm radial distance shown in the image region, but there are significantly more of them. It is interesting to note that the spatial distribution of the dry ejecta displays a starlike structure, similar in spacing to the ligaments produced in the sand-water slurry earlier in the event. The agglomerations of particles breaking off from the wetted mat can be seen to be released from the crater edge as it reaches its maximum radial diameter, rolling and bouncing across the sand surface. Few agglomerations are released but, due to their size, they make a considerable contribution to the mass transport away from the impact region. This contribution is quantified in Sec. VI.

IV. THREE-DIMENSIONAL PARTICLE TRACKING

In order to investigate the transfer of momentum to the sand particles, three-dimensional, time-resolved, particle tracking was used to measure the movement of the ejected particles after the droplet impact. For these measurements, three high-speed Photron SA3 cameras were used to record the impact event from three different angles simultaneously at a rate of 2000 frames per second and a resolution of 1024 by 1024 pixels. These spatially calibrated images were then used to triangulate the individual particle positions using the DAVIS software from LaVision. The cameras were mounted to look down on the sand bed at an angle of 60° to the surface and 120° from each other. Macro lenses with a 105-mm focal length were fitted to the cameras, providing an image region approximately 90 by 90 mm. Scheimflug mounts were used in conjunction with the lenses in order to create a focal plane parallel to the sand bed for each camera. With this experimental setup, and allowing for diffraction of the particle images, each of the 150–160-μm particles had a two-pixel diameter, allowing subpixel triangulation of position; i.e., less than ± 88 μm. Increasing the spatial resolution beyond this level was found not to yield a great improvement in positional accuracy. This lack of improvement was due to the nonspherical nature of the grains creating variation in the centroid position of each grain between camera images, thus limiting triangulation accuracy. Illumination of the scattered particles was provided by using pulsed LEDs, in

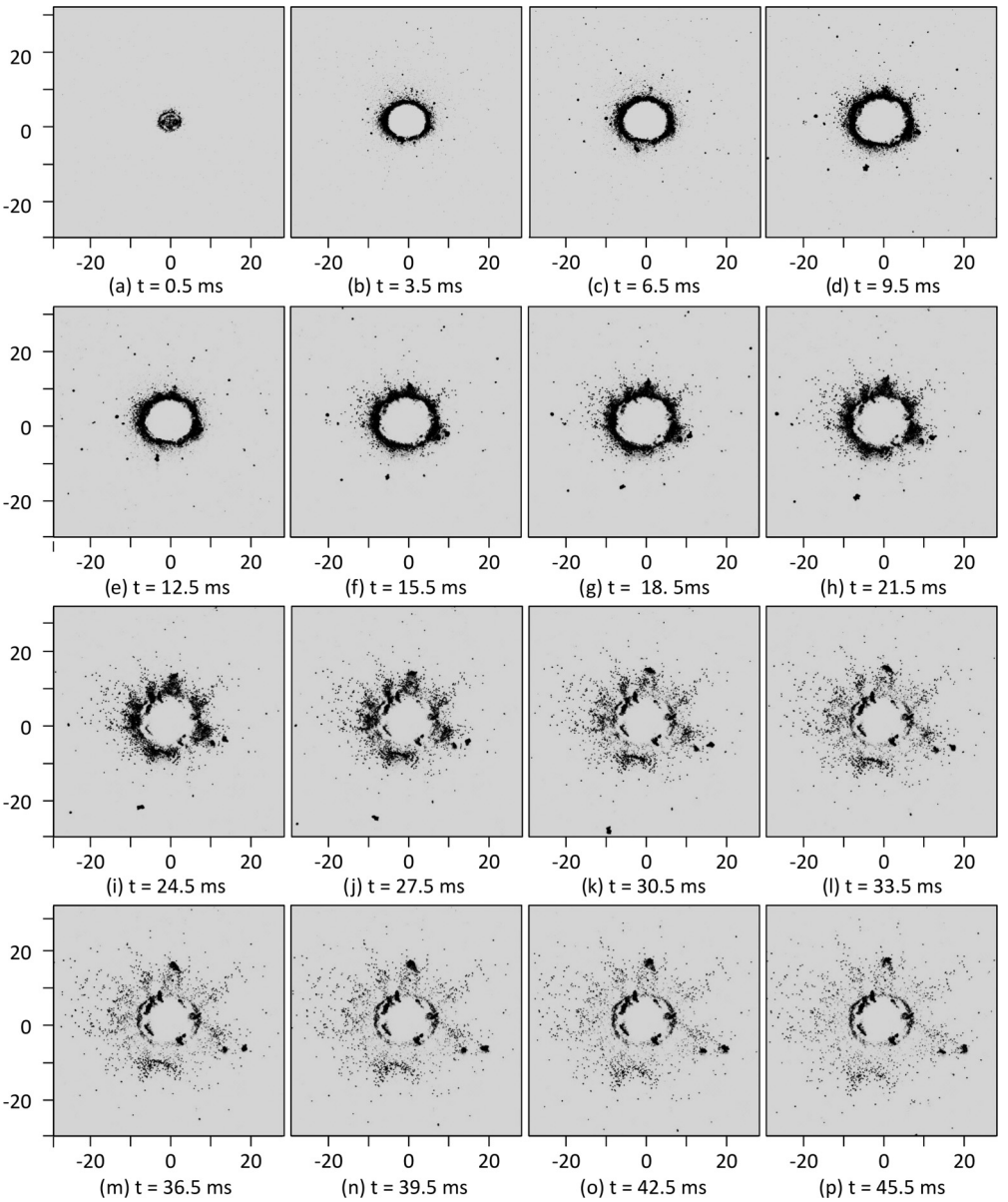

FIG. 3. Imaging of the ejecta from a 4-mm water droplet hitting a granular bed of 150–160-μm-diameter sand particles at a velocity of 6.5 m s^{-1}.

the same configuration as the ejecta imaging. The LEDs were synchronized to the frame rate of the cameras, with a pulse duration of 50 μs per frame. This arrangement resulted in clear images of the particles, with spatial movement between frames short enough to track their movement. An example of the resultant particle position tracks recorded can be seen in Fig. 4.

It can be seen from Fig. 4 that, due to the limitations of the image resolution required, some of the particle tracks leave the measurement region before the particles return to the bed surface. In addition, the region close to the point of particle ejection cannot be fully resolved due to the particle density, and some tracks contain breaks where crossing particles obscure a camera's viewpoint. In order to compensate for these issues, a MATLAB program was written to analyze each particle track and fit a third-order polynomial trajectory to its movement. This polynomial trajectory was then used to establish particle start position, first impact point of the particle returning to the bed, ejection angle, and ejection velocity. As shown in Fig. 5, a third-order fit to the particles' trajectory is required in order to take into account aerodynamic drag on the particles' motion, shifting it from a parabolic to a cubic arc.

The occurrence of particle bounce and secondary particle ejection is not investigated in this study; however, the recorded particle tracks demonstrate that such effects do significantly influence total particle-transport distances.

The particle tracks shown in Fig. 4 demonstrate two distinct types of movement: (a) high velocity, low ejection angle, high displacement; (b) low velocity, high ejection angle, low displacement. Plotting these two parameters of ejection velocity and angle against each other for each particle, as shown in Fig. 6, the two distinct populations present become

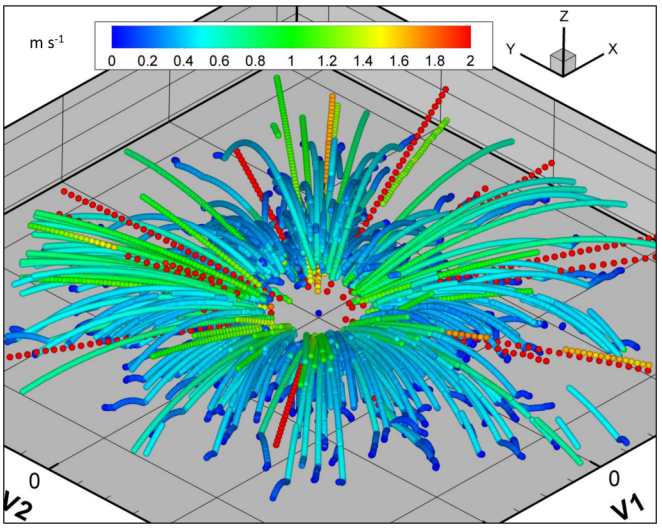

FIG. 4. (Color online) Particle-location tracks produced from a water droplet hitting a sand bed. Particles are colored by velocity in $\mathrm{m\,s^{-1}}$.

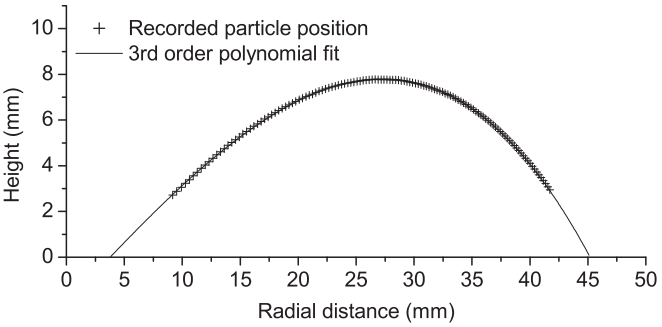

FIG. 5. Example particle motion with the corresponding third-order polynomial fit to its trajectory. Coefficient of determination $(R^2) = 0.999\,93$.

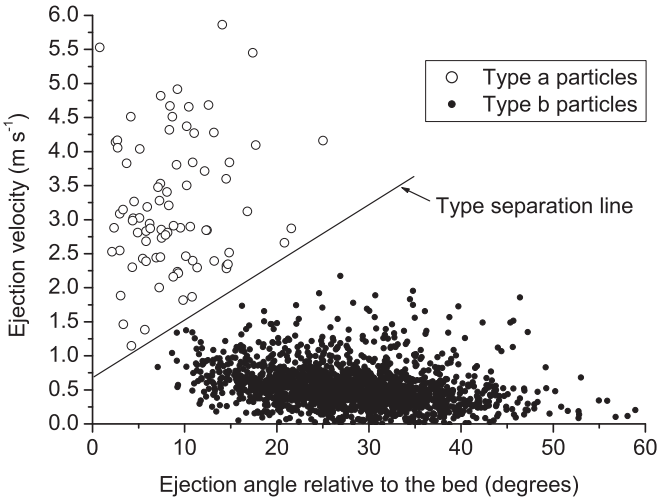

FIG. 6. Particle ejection velocity versus ejection angle, demonstrating the distinction between the ejection types.

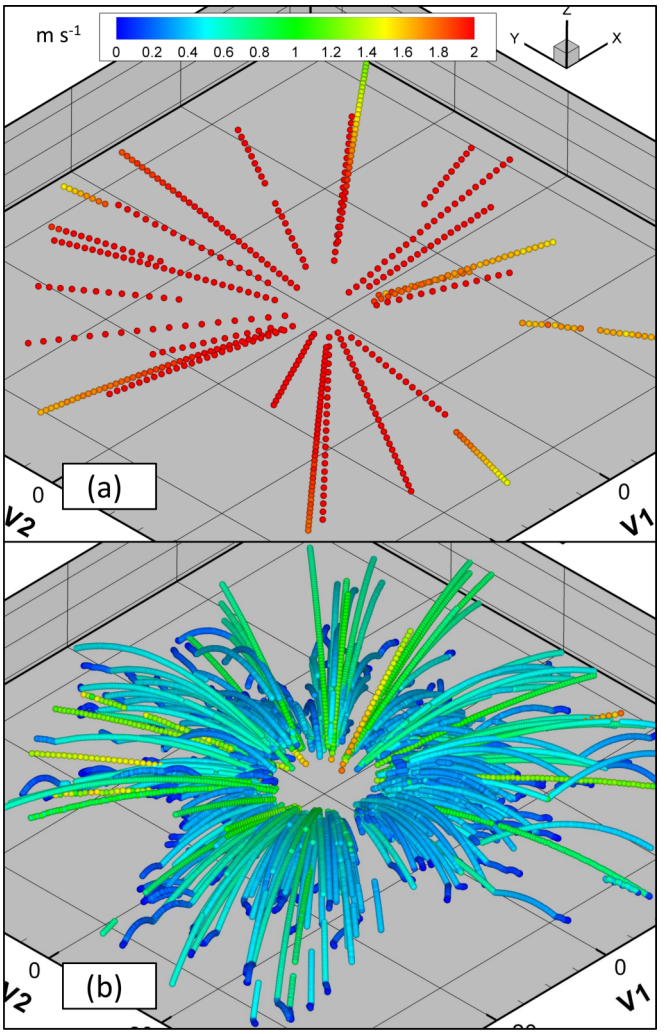

FIG. 7. (Color online) Particle location tracks according to particle type: (a) high velocity, low ejection angle, high displacement; (b) low velocity, high ejection angle, low displacement.

evident. The exact boundary between these populations is indistinct, so the position of the dividing line for the few ambiguous particles was chosen by taking ejection position into account; the type-a particles being ejected at positions closer to the center of the impact.

The two movement types are separated from each other and shown in Fig. 7. The two types of particle track identified are consistent with the imaging observations and correspond to the ejecta from the wetted sand region (type a) and dry particles ejected from the periphery of the impact crater (type b), which form an ejecta curtain. The early release of small splash droplets, as discussed in Sec. III B, are faintly visible in the recorded images, but are too intermittent to triangulate and so are filtered from the images prior to tracking. Due to the different mechanisms involved with the two different types of particle ejection, they are analyzed separately. The experiment was repeated four times; the number of particles tracks detected is shown in Table I.

The number of particle tracks recorded is consistent with the range of particle ejections recorded by Furbish *et al.* [9], who recorded an average of 584 particles ejected by a 3-mm

TABLE I. Particle track counts for each test carried out.

Test No.	No. of particles of type a	No. of particles of type b
1	26	862
2	25	1120
3	20	933
4	26	894
Average	24.25	952.25

droplet hitting a bed of 180-μm sand particles at a velocity of 7.2 m s^{-1} and 1800 particles for a 4-mm droplet hitting a bed of 180-μm sand particles at 7.6 m s^{-1}.

The results from the fitted particle tracks, for each of the experiments, have been combined and converted into frequencies relative to the total number of particles successfully tracked. These frequencies have then been normalized by the relevant bin width to aid data comparison. The average distributions for the dry particles ejected from the periphery of the crater (type b) are shown in Figs. 8 to 12.

The results from each of the four impact events produced very similar distributions, the average of which provided a clear profile of particle movement after impact. The profile of the particle ejection position (S), shown in Fig. 8, demonstrates that the ejection of the dry particles exhibits a Gaussian profile, with a mean ejection position (μ_S) of 5.14 mm from the center of the droplet impact and a standard deviation of (σ_S) 1.28 mm. Overlaid on the frequency histogram is the probability density function of Gaussian distribution calculated from μ_S and σ_S. The slight skew present in the frequency data, in comparison to the Gaussian probability density function (PDF), is believed to be a feature that would diminish with additional data sets. Due to this slight skew, the Kolmogorov-Smirnov goodness-of-fit test [17] for the Gaussian distribution produced a p value of only 0.03. It is interesting to note that the fluorescent images in Sec. III B show that the expanding mat of wet sand moves radially outwards up to distance of around 5 mm prior to breakup, the same position as the maximum particle ejection frequency.

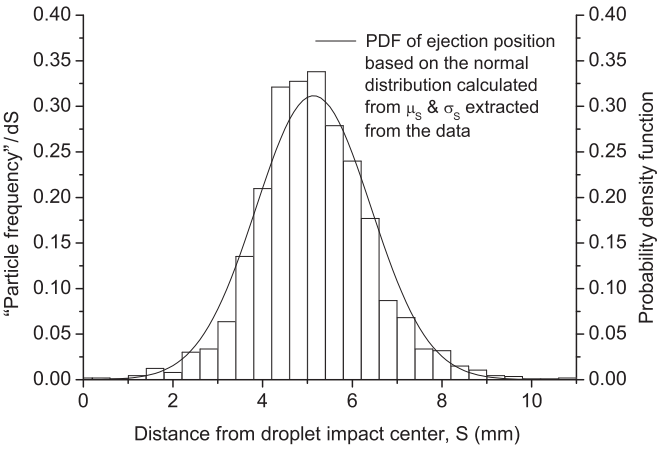

FIG. 8. Distribution of particle ejection position relative to the droplet impact center, type b.

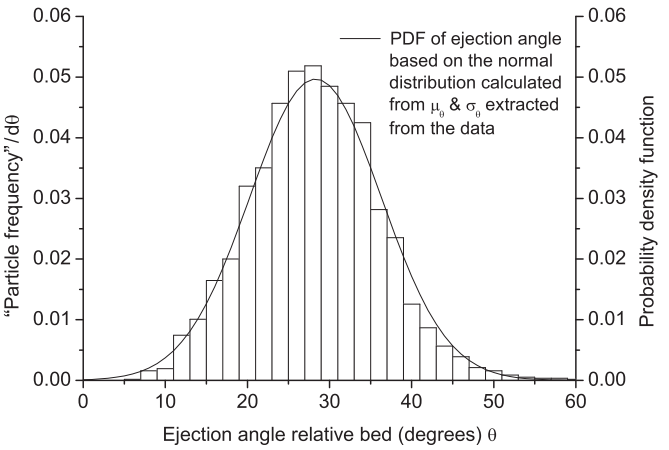

FIG. 9. Distribution of particle ejection angle relative to the bed surface, type b.

The angle of particle ejection relative to the bed surface (θ), shown in Fig. 9, also demonstrates a Gaussian profile with a mean (μ_θ) of 28.29° and a standard deviation (σ_θ) of 8.03°. The Gaussian PDF calculated from μ_θ and σ_θ demonstrates a good fit to the data with a Kolmogorov-Smirnov p value of 0.86. Comparing the particle ejection position to the ejection angle, as shown in Fig. 10, it can be seen there is a weak correlation between the two; the linear fit has a coefficient of determination (R^2) of 0.30. Particles that leave the bed surface close to the droplet impact center, early on in the development of the impact crater, have a lower ejection angle compared with those that are ejected further out when the crater is more fully developed.

The distances the particles travel from their ejection position to the point where they first return to the bed are shown in Fig. 11; these distances do not include any further rebound of the particles or rolling across the surface. The frequency of the distance traveled by the particles demonstrates a long-tail distribution, with some particles travelling up to 140 mm from the droplet impact center. The arithmetic mean of the travel distance from all four tests is 19.69 mm and the

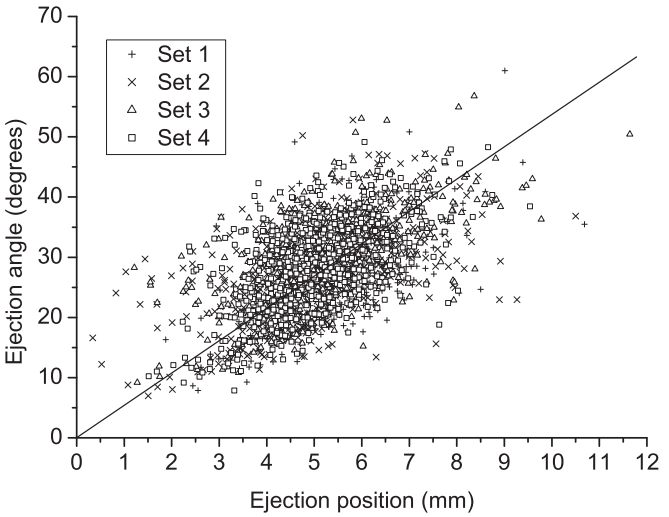

FIG. 10. Particle ejection angle relative to ejection position.

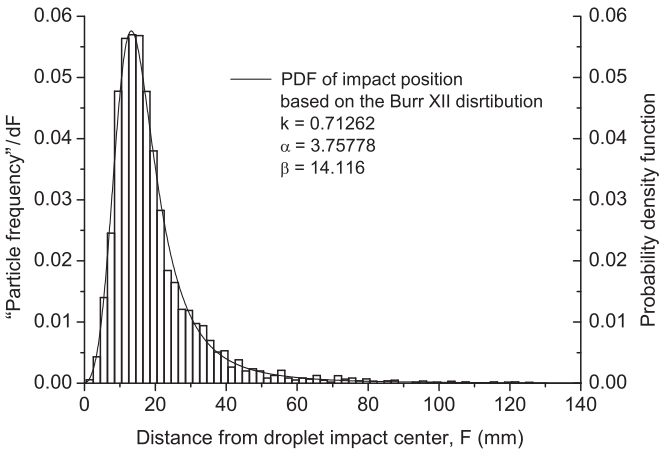

FIG. 11. Distribution of particle impact travel distance, type b.

arithmetic standard deviation is 14.47 mm; the geometric mean is 16.13 mm and the geometric standard deviation is 1.855.

In the light of the asymmetric nature of the travel distance distribution, whose precise shape we have no *a priori* information on, and that simple distribution functions (e.g., log-normal) do not provide significant fits to the data, we have chosen to fit the Burr XII distribution [18] to the data [as given in Eq. (1)]. The Burr XII distribution fits the data significantly in all cases and has good applicability to simulation modeling [19]. The Burr XII has two shape parameters, k and α, a scale parameter β, and a location parameter γ:

$$f(x) = \frac{\alpha k\left(\frac{x-\gamma}{\beta}\right)^{\alpha-1}}{\beta\left[1+\left(\frac{x-\gamma}{\beta}\right)^{\alpha}\right]^{k+1}}. \quad (1)$$

For the distribution overlaid in Fig. 11 the shape parameter k is equal to 0.712 62, the shape parameter α is equal to 3.757 78, the scale parameter β is equal to 14.116, and the location parameter γ is equal to 0. The Burr distribution exhibits a high level of fit to the particle travel data; using the Kolmogorov-Smirnov goodness-of-fit test, the fit was found to have a p value of 0.84.

The ejection velocity of the particles, as extrapolated from the particle trajectories, is shown in Fig. 12. The profile of the ejection velocity demonstrates a profile similar to that of the particle travel distance, that of a long-tail distribution. The peak of the distribution occurs around the geometric mean, 0.48 m s^{-1}, with particles being released at velocities up to 2 m s^{-1}. The similarity in profile between ejection velocity and transport distance indicates that the variation in ejection velocity is a primary cause of the long-tail distribution seen in the transport data. The arithmetic mean of the ejection-velocity data is 0.55 m s^{-1}, the standard deviation is 0.32 m s^{-1}, and the geometric standard deviation is 1.78. The Burr XII distribution, as used for the transport distance data, also provides a good fit to the particle ejection velocity, as shown in Fig. 12, with the shape parameter k equal to 1.189, the shape parameter α equal to 3.917, the scale parameter β equal to 0.647, and the location parameter γ equal to -0.111; the Kolmogorov-Smirnov goodness-of-fit [16] test returns a p value of 0.05. It is to be expected that a weaker fit to the velocity data will occur as there are higher inaccuracies present in the velocity calculation; slight variations in the particle positions recorded have little impact on the fitted trajectories but have a greater impact on the velocity calculation. Such inaccuracies directly influence the extrapolated ejection velocity, affecting the distribution profile.

The distributions for the type-a ejected particles, those released from the wetted sand region, are shown in Figs. 13 to 16. These particles display quite different characteristics from those of the dry sand particles (type b). The number of ejected particles is small for each event, around 24 particles, so statistical fits are not included in the analysis. However, the general trends produced provide good information about the particle behavior.

The distribution of ejection position for the type-a particles is shown in Fig. 13. This distribution demonstrates that the origins of the particle trajectories, where their paths intersect the bed surface, occur much closer to the impact center of the droplet than the type-b particles, many of them from within the droplet radius itself. It is interesting to note that a peak

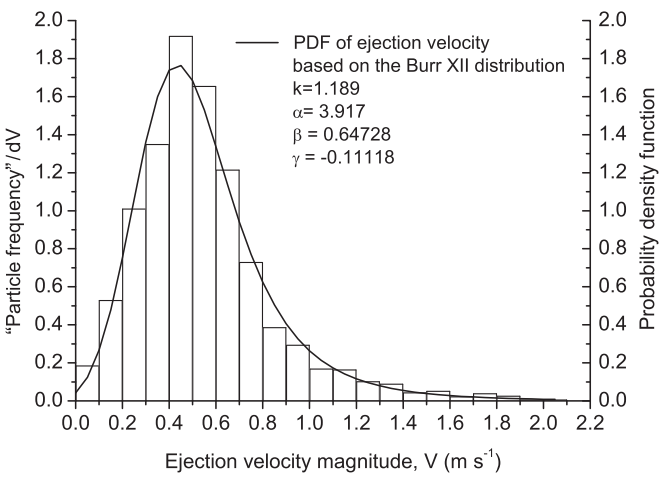

FIG. 12. Distribution of particle ejection-velocity magnitude, type b.

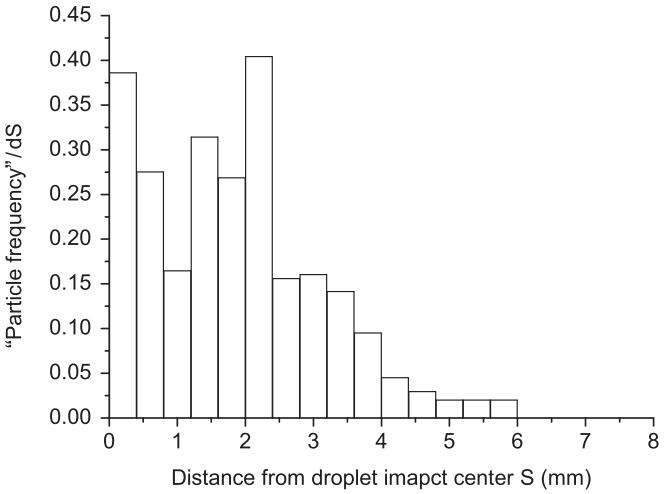

FIG. 13. Distribution of particle ejection position relative to the droplet impact center, type a.

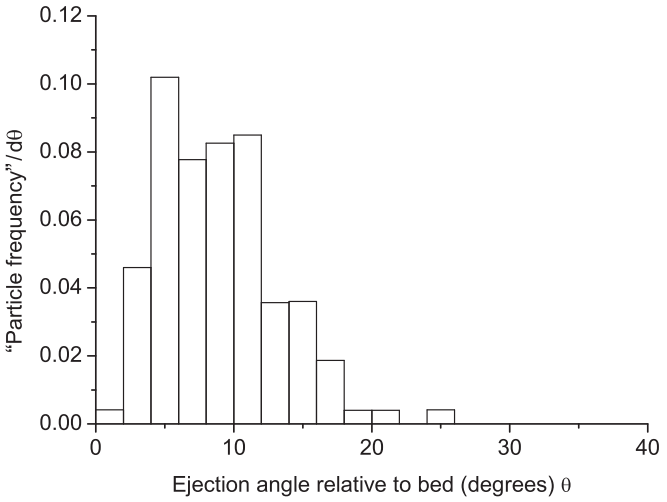

FIG. 14. Distribution of particle ejection angle relative to the bed surface, type a.

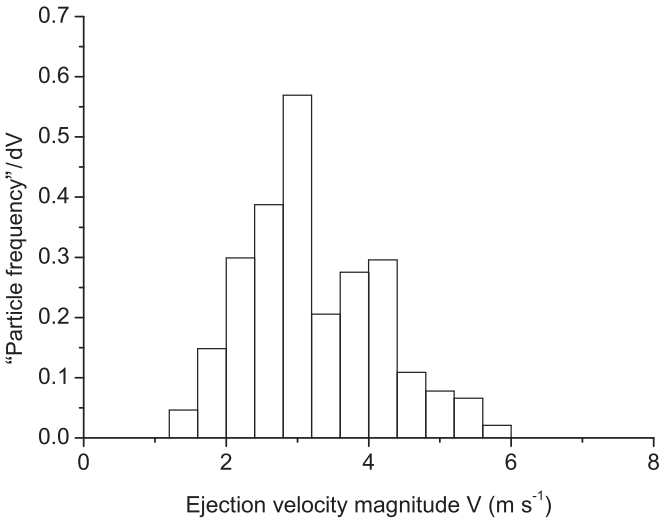

FIG. 15. Distribution of particle ejection-velocity magnitude, type a.

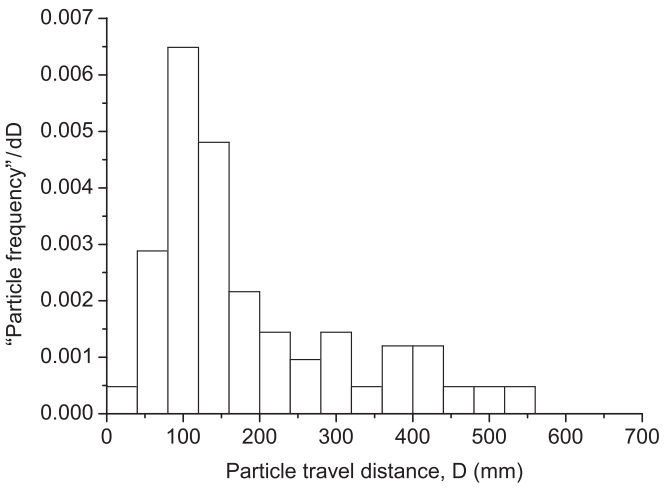

FIG. 16. Distribution of particle impact radial position, type a.

in ejection position occurs just outside of the droplet radius, indicating that the release of ejecta occurs as the wet mat is expanding, as observed in Fig. 2.

Figure 14 displays the ejection angle distribution for type-a particles. These data clearly show that the type-a particles leave the bed at much lower angles than type b, with a mean of just 9° to the bed and a maximum of only 25°. This shallow angle indicates that type-b particles are driven by the lateral motion of the deforming droplet, the downward motion of which is arrested by the static granular bed, rather than a reaction from the bed due to grain displacement.

The ejection velocity of type-a particles, as shown in Fig. 15, is significantly higher than recorded for type-b particles, with an average of 3.16 $\mathrm{m\,s^{-1}}$. This high ejection velocity demonstrates that there is a greater efficiency in the momentum transfer for these particles than those of type-b. This more effective transfer of energy, due to the direct interaction between water and particle, means that, despite the few particles involved, an appreciable portion of the droplet energy is still transferred to this form of particle ejection.

As a result of the high ejection velocity of type-a particles, the distance they travel is considerably higher than that traveled by type-b particles. The travel distances, shown in Fig. 16, have a broad distribution ranging from 35 mm up to 550 mm, with a peak occurring in the 100–150-mm range. The average impact position is 189 mm. These large travel distances mean that the type-a form of particle ejection has a considerable impact on overall transport of the granular media due to the droplet impact.

V. PARTICLE EJECTION

Both imaging of the droplet impact and three-dimensional tracking of the subsequent ejecta have demonstrated that two distinct mechanisms of particle ejection occur for this interaction: type a and type b. Type-b particles represent the main ejecta curtain produced as particles are sheared from the surface of the depression during expansion of the impact crater; this process is discussed in more detail later in this section. Type-a particles, however, are ejected by a different process, whereby they interact directly with the water droplet; it has been shown in Sec. IV that these particles are characterized by high ejection velocities and low ejection angles. For the impact of solid objects, in addition to the ejecta curtain, two other mechanisms of particle ejection have been reported in the literature, both of which are referred to as *jetting*. The first form of jetting is caused by the collapse of a void formed in the granular medium as the impacting object penetrates below the surface. The subsequent void collapse causes a near-vertical release of particles [20,21,22,23]. The second form of jetting occurs when an impacting object hits a surface at high speed and low angle, releasing a small quantity of particles on impact [24]. Clearly neither of these mechanisms fit with the behavior of the type-a particles reported in this study as (a) no appreciable void is formed in the granular bed (see Fig. 1), (b) the particles are released at a low angle, and (c) the droplet lands perpendicular to the bed surface. In difference to solid object impacts, the source of the type-a particle ejection is the breakup of the droplet as it impacts the

granular medium, stripping particles from the edge of the wet mat, as described in Sec. III.

The transition between splashing and nonsplashing droplets has been studied in detail by several studies, with the splashing parameter (K_d) often used to separate the two regimes [25,26]. The splashing parameter K is a combination of the Weber number and the Reynolds number where

$$K = \mathrm{We}^{1/2}\mathrm{Re}^{1/4} = \left(\frac{\delta^3 D_O^3 U^5}{\mu\gamma^2}\right)^{1/4},$$

where δ is density, D_O is diameter, U is impact velocity, μ is viscosity, and γ is surface tension.

The higher the splashing parameter is, the greater the propensity for droplet breakup. The threshold between splashing and nonsplashing (K_d) has been reported to vary according the surface: For a smooth surface $K_d = 57.7$ [25], for a bed of 5-μm fibers $K_d = 87$ [27], and for a bed of 81-μm glass spheres $K_d = 120$ [12]. The impacting droplet in this work has a splashing parameter $K = 556$, a value far exceeding these thresholds, indicating its propensity to splash. However, the penetration of the water into the granular medium is so rapid (within 1 ms of impact; see Fig. 2) the water has already started to mix with the sand grains as breakup occurs. This occurrence results in the splash detachment of sand grains with the water at a low angle to the bed. A study by Marston *et al.* [28] observed that for a fine granular bed (0–53-μm diameter), both bed surface and impact velocity strongly influence the penetration of an impacting drop and the generation of satellite droplets due to splash; adjustment of these two parameters to investigate their influence on type-a and type-b ejecta would be an interesting expansion to this work.

With regard to the to the type-b particles, which make up the ejecta curtain, it is clear that there are direct comparisons with the ejecta recorded for solid object impacts, indicating that similar processes are involved. In Fig. 17 the relationship between ejection position and velocity is compared with results for solid object impact produced by Yamamoto *et al.* [29] using scaling laws, as presented by Housen and Holsapple [30]. The ejection velocity of the particles (v) is scaled to the impact object velocity (U); the ejection position (s) is scaled to the impact object radius (a) and the ratio between the bulk density of the granular bed (ρ) and the impact object density (δ) by the formula: $(s/a)(\rho/\delta)^{\nu}$. The exponent ν has been shown in literature to be consistently equal to 0.4, regardless of the materials involved [30]. The average ejection position and particle velocity from this study are shown. The data presented by Yamamoto *et al.* [29] were collected for a polycarbonate sphere impacting a bed of glass microspheres. It is evident from this scaled comparison that, despite the differences in the materials, the same power-law relationship holds for both experiments. Other results presented for solid object impacts into glass spheres and sand presented by Housen and Holsapple [30] show a similar power-law relationship, but a factor of 3 below the Yamamoto *et al.* relationship. However, these other experiments were all conducted at significantly higher impact velocities (1400–1900 m s^{-1}), which may explain the disparity.

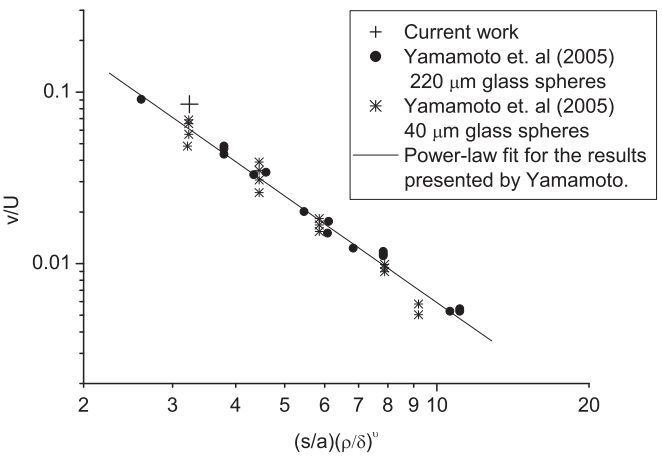

FIG. 17. Scaled relationship between particle ejection velocity and ejection position, a comparison between the current work and data produced from solid object impacts.

Despite the similarity in scaled velocity relationship between this droplet experiment and those using solid objects, there is a significant difference in terms of ejection angle. For solid object impacts at low velocity (1 to 4 m s^{-1}) using spheres of different radii on 400-μm glass spheres, Deboeuf *et al.* [6] recorded the ejecta sheet angle to be consistently between 45° and 60°. Similarly, Marston *et al.* [31] state that after the early stages of solid sphere impact onto 520-μm glass beads, the particle ejection reaches a constant of 45° to 50°. However, the average angle of particle ejection for this study is 30°, significantly lower than the solid object cases. This lower angle is thought to be a result of the rapid penetration of the water into the sand bed, resulting in a much shallower crater relative to its diameter. The crater profile is looked at in more detail in Sec. VII.

VI. MOMENTUM TRANSFER

It is evident from the particle tracking data that the two mechanisms of particle ejection, a and b, release different numbers of particles with significantly different velocities and trajectories. For type-b particles, an average of 952 particles is released from each droplet impact, with an average velocity of 0.55 m s^{-1}. Given that the average particle diameter is 155 μm and assuming they are approximately spherical with a density equivalent to pure silica (2648 kg m^{-3}), the average momentum of a type-b particle is 2.86×10^{-9} N s. This average particle momentum results in a total momentum of 2.72×10^{-6} N s per droplet impact, which is 1.79% of the momentum of the 3.6-mm droplet as it impacts the bed at 6.45 m s^{-1}. For the type-a particles, an average of 24 particles are released from each droplet impact, with an average velocity of 3.16 m s^{-1}. Making the assumption that each of the type-a particles consists of a single sand grain held in a sphere of water, and ignoring the water component, the average momentum of each particle is 1.63×10^{-8} N s. This provides a total momentum of 3.95×10^{-7} N s per droplet impact associated with type-a sand particles, which is 0.26% of the droplet momentum on impact. Combining the results from type-a and type-b ejections, a total of 2.05% of the momentum of the droplet is transferred to the ballistic ejection of sand particles. The detail of this momentum transfer is summarized in Table II.

TABLE II. Momentum transfer between the water droplet and the ejected sand particles.

	Drolpet	Type a	Type b
Average No. of particles	1	24.25	952.25
Average diameter	3.56 mm	155 μm	155 μm
Average mass	2.36×10^{-5} kg	5.16×10^{-9} kg	5.16×10^{-9} kg
Average velocity	6.45 m s^{-1}	3.16 m s^{-1}	0.55 m s^{-1}
Average particle momentum		1.63×10^{-8} N s	2.86×10^{-9} N s
Total momentum	1.52×10^{-4} N s	3.95×10^{-7} N s	2.72×10^{-6} N s
Percentage of droplet momentum		0.26%	1.79%

The total momentum transferred to the ballistic ejection of particles is small in comparison to the momentum of the impacting droplet. The rest of the droplet energy is transferred to aspects such as deformation of the bed, compression of the grain packing, and movement of wet sand conglomerates across the bed surface. To investigate these aspects, surface profiling of the granular bed postimpact was carried out.

VII. SURFACE PROFILING OF THE IMPACT CRATER

In order to measure the surface profile of the impact crater, without disturbing the granular bed, photogrammetry was employed. Multiple stereo photographs were taken of the bed surface using a Nikon 3100 digital camera fitted with a Nikkor 105-mm macro lens. Each image taken, with a resolution of 4608 by 3072 pixels, corresponded to a bed area of approximately 54 by 36 mm. The multiple images were combined to cover an 80-by-80-mm region centered on the droplet impact with a 50% area overlap between image pairs. PHOTOMODELER scanner software produced by EOS systems was used to process the images and provide the surface height data; subsequent analysis was carried out in MATLAB. This arrangement of imaging and processing resulted in heights calculated across the bed surface with a grid spacing of 100 μm and surface features resolvable down to a step change of 100 μm. A surface profile map with heights represented in grayscale is shown in Fig. 18.

The surface map in Fig. 18 shows clearly several of the features seen in the impact imaging. The impact crater itself is identifiable by a central depression surrounded by a raised circular rim of dry sand. Within this rim, the uneven edge of the wet-mat region is apparent, lining the crater. This wet mat can be seen to have broken up slightly with several deep fissures within it, resulting in parts of the mat protruding higher than the dry sand rim. Out from the crater itself, agglomerations of the granular medium can be seen sitting on the bed surface where they have become detached from the wet-mat region. Slight indentations are recorded in the bed surface where these agglomerations have skipped across the surface before coming to rest.

From the three-dimensional surface profiles, two-dimensional sections through the impact crater were extracted. Figure 19 shows the x- and y-axis sections through the droplet impact center for the Set 3 crater; there is a 1:10 scale ratio between the radial distance and the height in order to show the details clearly. To the right of the origin of this graph, there is a noticeable discontinuity between the x and the y profiles where part of the wet mat has broken away in the y axis; from this difference in the profiles it can be seen that the water has penetrated approximately 1.5 mm deep into the sand at the crater's edge, equivalent to around 10 grain diameters. On the negative side of both x and y profiles, a double peak can observed: the outer peak reaching to around 0.25 mm associated with the circular rim of dry sand and the inner peak rising to around 0.7 mm associated with the wet-mat region.

In order to provide an overview of the crater morphology, average profiles for each of the impact craters were calculated (shown in Fig. 20). These profiles were produced by taking multiple sections through the crater from the impact center outwards at 5° rotations and then calculating the average from these 72 sections. Comparing the four impact events, it can be seen that the shapes of the rotationally averaged crater profiles are all very similar. All of the craters have a raised rim around the depression, with each rim averaging 0.3 mm in height and 7.5 mm in radius. The sides of the craters themselves are straight sided, and the base of the depression is around 0.7 to 0.8 mm below the bed surface. At the base of each crater, instead of a smooth continuation of the profile, there is a peak slightly larger in diameter than the impacting droplet.

Such raised peaks within a crater have been observed in impacts between solid objects and granular beds [3,20] and have been attributed to granular jets produced by void formation and collapse as the object penetrates below the

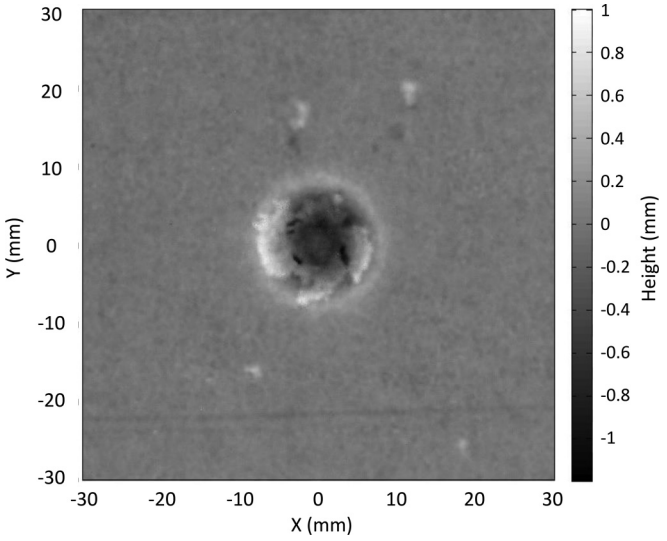

FIG. 18. Surface profile of Set 3 droplet crater measured using photogrammetry; heights shown in grayscale with a grid spacing of 100 μm.

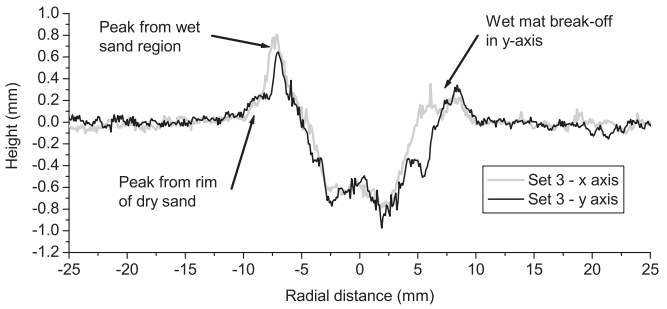

FIG. 19. Surface profile section of Set 3 droplet crater in x and y directions through the crater center.

surface [20,21,22]. In addition, central peaks are a common feature of meteorite impact craters, where their formation is attributed to the inward collapse of a simple transient crater formed during impact [32]. The exact mechanism of the central peak formation found in this study is unclear. However, it is evident that, while a true void is not formed, initial displacement of the sand grains by the water on impact, followed by further infiltration, could result in subsequent collapse of the crater and peak formation. Further work would be required to investigate this process.

The diameter of the final crater produced, in relation to the droplet impact parameters, is compared with data produced from solid object impacts in Fig. 21. As used in other work, such as Holsapple [33], Schmidt [34], and Yamamoto *et al.* [35], two dimensionless scaling parameters have been used as the basis of this comparison: the scaled crater radius (Π_R), which is equal to $(\rho/m)^{1/3}$ $(D_f/2)$, and the gravity scaled size of the impacting object, which is equal to 3.22 (g/U^2), where ρ is the bulk density of the granular bed, m is the mass of the impacting object, D_f is the diameter of the crater, g is the gravitational acceleration, is the radius of the impacting object, and U is the velocity of the impacting object.

The relationship between the scaled crater radius and the scaled impact object size produced from this work is in good agreement with the power-law relationship evident in the results presented by Mizutani *et al.* [36] for aluminum sphere impacts onto sand. Despite the work by Mizutani *et al.* involving higher velocities (70 to 830 m s^{-1}) and using solid impact objects, the bulk material is very similar in terms

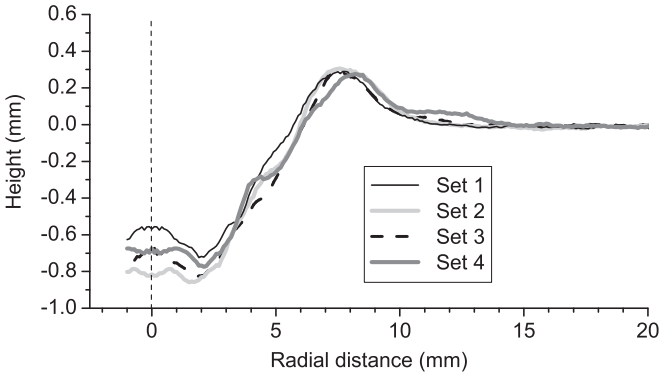

FIG. 20. Average surface profiles of the craters produced from all four droplet events.

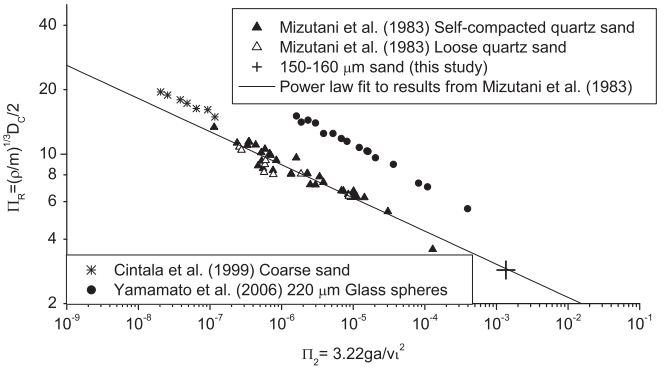

FIG. 21. Relationship between the scaled crater radius and the gravity scaled size, a comparison between the current work and data produced from solid object impacts.

of material (quartz sand), particle size (0 to 250 μm, with majority being 150 to 250 μm), and bulk density (1360 and 1590 kg m^{-3} for loose and compacted, respectively); it is this similarity which may be the cause of the agreement. Results produced by Yamamoto *et al.* [35] for comparable test conditions present a similar power-law relationship but offset from the data by Mizutani *et al.* and this study by a factor of 1.8. Yamamoto *et al.* suggest that this discrepancy between their results and those presented by Mizutani *et al.* is due to the differences in target material properties, which was a bed of glass spheres as opposed to sand. This offset in the data is interesting considering that the average ejection velocity to position relationship of the current study matches the experiments by Yamamoto *et al.*, regardless of the shape of the particles, but the final crater radius does not. Results produced by Cintala *et al.* [37] also show a similar power-law relationship, only slightly offset from the Mizutani *et al.* relationship. These experiments were conducted at much higher velocities (800 to 1920 m s^{-1}) onto coarse sand ranging from 1 to 3 mm in diameter, with a bulk density of 1510 kg m^{-3}. The similarity in granular medium and power-law relationship reinforces the idea that the particle properties influence the crater size relationship. Clearly, more research is required to resolve the reasons for the similarities and differences observed in the measured data. It is significant, however, that although the water droplet deforms on impact and penetrates into the granular bed, there are striking similarities to solid object impact.

Similar to the scaling parameters used by Holsapple [33], Schmidt [34], and Yamamoto [35], Katsuragi [38] presented a scaling law relating crater diameter to both the impactor and bed properties for low-velocity water-droplet impacts, the main difference being the inclusion of the droplet properties by Katsuragi via the Weber number. For a 4.8-mm water droplet impacting upon different granular beds (ranging from 4 to 50 μm in grain diameter), Katsuragi demonstrated a relationship held for low Weber numbers,

$$\frac{D_f}{D_O} \cong 0.5\frac{\rho}{\rho_w}\mathrm{We}^{1/4},$$

where D_f is crater diameter, D_O is droplet diameter, ρ is bulk density of the granular bed, ρ_w = density of the droplet, and

TABLE III. Average size and position of the agglomerates that have broken off from the wet-mat region for each data set.

	No. of agglomerates	Average distance from droplet impact (mm)	Average volume of each agglomerate (mm^3)	Average No. of grains in each agglomerate	Total No. of grains in agglomerates
Set 1	5	21.11	1.86	475.17	2375.86
Set 2	4	25.60	0.84	213.31	853.26
Set 3	6	42.29	0.76	193.52	1161.12
Set 4	6	26.08	1.65	421.12	2526.70
Average	5.25	28.77	1.28	325.78	1729.23

We is the Weber number. For the experiment detailed in this study, the diameter ratio between the crater and the droplet was 4.21 and the dimensionless number $(\rho/\rho_w)\mathrm{We}^{1/4}$ was equal to 8.8, supporting Katsuragi's scaling law.

With regard to the ratio between crater diameter and depth, the water-droplet impact in this study produces distinctly different results to solid object impacts. The experiments carried out by Yamamoto *et al*. [35] looking at polycarbonate projectiles hitting a bed of glass microspheres produced average depth to diameter ratios of between 0.11 and 0.14, depending on the glass bead diameter. Likewise, for aluminum projectiles impacting a bed of quartz sand, Mizutani *et al*. show a linear relationship between crater depth and diameter of 0.15 for compacted sand and 0.26 for loose sand. For this study of a water droplet hitting and bed of loose sand, a much lower ratio of 0.05 exists between depth and diameter. This disparity is believed to be due to the rapid penetration of the water into the sand bed, whereby the water moves around the grains as well as displacing them, resulting in little vertical movement of the bed. This shallow crater formation indicates that crater depth is not governed by the same relationships as solid objects such as those proposed by Katsuragi and Durian [39].

In addition to the crater morphology, the surface profiling also provides details of the size and position of the agglomerates which break off from the main wet mat. A summary of the average agglomeration size and position for the different datasets is given in Table III. The number of grains present in each agglomeration is estimated by multiplying the measured agglomeration volume by the packing density (0.5) and dividing by the average volume of a sand grain, assuming an approximately spherical profile.

The limitation in the number of events recorded means that meaningful statistics cannot be drawn from the agglomeration data; however, useful information on the interaction is still evident. Few agglomerations break off from the crater as they receive momentum from the radially expanding water, but their size means that they contribute significantly to the transport of grains away from the impact site. The total number of grains moved in this manner is on average almost twice that of the ballistic grains and their radial movement similar in terms of average distance. It is interesting to observe that the events with the fewest grains present in transported agglomerates also have the highest number of ballistic particles, suggesting slight differences in energy distribution between events. The average distance the agglomerates move is fairly consistent between the datasets with the exception of Set 3; this set has two small agglomerations, less than 1 mm^3 in volume, which travel around 80 mm from the droplet impact, significantly increasing the mean transport distance.

Given that the average number of grains found in the agglomerations was almost twice that of the ballistic grain particle count and that their transport distance was, on average, ~29 mm, a significant portion the droplet momentum must have been transferred to their movement. Although the exact agglomeration ejection velocities were not recorded, their displacements indicate that their combined momentum at release could be up to twice that of the ballistic particles.

VIII. CONCLUSION

The interaction that occurs between an impacting water droplet, 3.6 mm diameter, and a granular bed of dry sand particles, 150–160 μm in diameter, has been experimentally investigated using high-speed imaging, three-dimensional particle tracking, and photogrammetric surface profiling techniques. The results from this work have shown that, in addition to liquid splash as the droplet strikes the granular bed, two distinct mechanisms are involved in ejecting granular particles from the bed:

(a) the ejection of water-encapsulated particles from the edge of the wet mat produced as the droplet penetrates the bed and spreads radially outwards;

(b) the ejection of dry sand from the periphery of the crater as the granular bed is deformed by the droplet impact.

The first ejection mechanism has been shown to involve few particles (an average of 24), but it transports them a long way in comparison to the second mechanism (an average of 173 mm from the droplet center). The trajectories from this form of ejection are characterized by high ejection velocities (an average of 3.16 m s^{-1}) and low ejection angles (an average of 9°). The second ejection mechanism releases significantly more particles than the first (an average of 952 particles) but is characterized by higher ejection angles (an average angle of 28°) and slower ejection velocities (an average of 0.55 m s^{-1}). The distance traveled by these second-mechanism particles demonstrates a long-tail distribution, which is accurately represented by the Burr XII distribution. The ejection-velocity distribution demonstrates a similar profile. Considering both mechanisms of ballistic particle ejection, the tracking data have shown that despite the high numbers of particles involved, only ~2% of the droplet's momentum is transferred to this form of granular transport.

Comparing the droplet impact results to impacts involving solid objects, the relationship between scaled average particle

ejection velocity and scaled ejection position follows the same power-law trend reported for low-velocity impacts. However, ejection angle of the ejecta curtain is significantly lower in comparison to solid object impacts. This lower angle is thought to be a result of the rapid penetration of the water into the sand bed, which results in a much shallower crater relative to its diameter in comparison to solid object impact.

In terms of the morphology of the bed surface produced by the droplet impact, the photogrammetric profiling has shown that the average crater shape is highly repeatable. The crater produced, for this interaction, is shallow (only ~0.8 mm deep), with a wide diameter approximately 4 times that of the impacting droplet. The data have shown that a raised peak occurs at the center of the crater; however, the exact mechanisms involved in its formation are unclear. The relationship between the scaled crater radius and the gravity scaled size of the impacting droplet fits along the same power-law relationship found for solid object impacts into a granular bed of similar properties.

Agglomerations of particles, which break off from the wet mat produced by the water penetration, have been shown to be a significant mechanism in material transport. These agglomerations move, on average, almost twice as many particles as the ballistic processes, with a transport distance comparable to the arithmetic mean of the ballistic particles. As such, the momentum of the agglomerates on release could be up to twice that recorded for the ballistic particles. Thus, it is suggested that approximately 4% of droplet moment is transferred to particle motion of both types of transport.

ACKNOWLEDGMENT

This research was supported by NERC Grant No. NE/H006176/1.

[1] M. Hou, Z. Peng, R. Liu, K. Lu, and C. K. Chan, Phys. Rev. E **72**, 062301 (2005).
[2] D. I. Goldman and P. Umbanhowar, Phys. Rev. E **77**, 021308 (2008).
[3] A. M. Walsh, K. E. Holloway, P. Habdas, and J. R. de Bruyn, Phys. Rev. Lett. **91**, 104301 (2003).
[4] S. J. de Vet and J. R. de Bruyn, Phys. Rev. E **76**, 041306 (2007).
[5] J. F. Boudet, Y. Amarouchene, and H. Kellay, Phys. Rev. Lett. **96**, 158001 (2006).
[6] S. Deboeuf, P. Gondret, and M. Rabaud, Phys. Rev. E **79**, 041306 (2009).
[7] E. J. Gabet and T. Dunne, Water Resour. Res. **39**, 1002 (2003).
[8] L. Mouzai and M. Bouhadef, J. Hydraul. Res. **41**, 61 (2003).
[9] D. J. Furbish, K. K. Hamner, M. Schmeeckle, M. N. Borosund, and S. M. Mudd, J. Geophys. Res. **112**, F01001 (2007).
[10] H. Ghadiri, Earth Surf. Process. Landforms **29**, 77 (2004).
[11] G. Delon, D. Terwagne, S. Dorbolo, N. Vandewalle, and H. Caps, Phys. Rev. E **84**, 046320 (2011).
[12] Nefzaoui and O. Skurtys, Exp. Therm. Fluid. Sci. **41**, 43 (2012).
[13] H. Katsuragi, J. Fluid. Mech. **675**, 552 (2011).
[14] A. J. Parsons and A. M. Gadian, Earth Surf. Process. Landforms **25**, 723 (2000).
[15] R. Gunn and D. Z. Kinzer, J. Meteor. **6**, 243 (1949).
[16] H. Marmanis and S. T. Thoroddsen, Phys. Fluids **8**, 1344 (1996).
[17] R. B. D'Agostino and M. A. Stephens (eds.), *Goodness of Fit Techniques* (Marcel Dekker, New York, 1986).
[18] I. W. Burr, Ann. Math. Stat. **13**, 215 (1942).
[19] P. R. Tadikamalla, Int. Stat. Rev. **48**, 337 (1980).
[20] D. Lohse, R. Bergmann, R. Mikkelsen, C. Zeilstra, D. van der Meer, M. Versluis, K. van der Weele, M. van der Hoef, and H. Kuipers, Phys. Rev. Lett. **93**, 198003 (2004).
[21] J. R. Royer, E. I. Corwin, A. Flior, M.-L. Cordero, M. L. Rivers, P. J. Eng, and H. M. Jaeger, Nat. Phys. **1**, 164 (2005).
[22] J. R. Royer, B. Conyers, E. I. Corwin, P. J. Eng, and H. M. Jaeger, Europhys. Lett. **93**, 28008 (2011).
[23] S. T. Thoroddsen and A. Q. Shen, Phys. Fluids **13**, 4 (2001).
[24] W. Yang and T. J. Ahrens, Icarus **116**, 269 (1995).
[25] C. H. R. Mundo, M. Sommerfeld, and C. Tropea, Int. J. Multiphase Flow **21**, 151 (1995).
[26] A. Yarin, Annu. Rev. Fluid Mech. **23**, 159 (2006).
[27] A. Lembach, H. Tan, I. Roisman, T. Gambaryan-Roisman, Y. Zhang, C. Tropea, and A. Yarin, Langmuir **26**, 9516 (2010).
[28] J. O. Marston, S. T. Thoroddsen, W. K. Ng, and R. B. H. Tan, Powder Technol. **203**, 223 (2010).
[29] S. Yamamoto, N. Okabe, S. Sugita, and T. Matsui, *Proceedings of the 36th Lunar Planetary Science XXXVI Conference* (Lunar and Planet. Inst., League City, Texas, 2005), p. 1600.
[30] K. R. Housen and K. A. Holsapple, Icarus **211**, 856 (2011).
[31] J. O. Marston, E. Q. Li, and S. T. Thoroddsen, J. Fluid Mech. **704**, 5 (2012).
[32] H. J. Melosh and B. A. Ivanov, Annu. Rev. Earth Planet. Sci. **27**, 385 (1999).
[33] K. A. Holsapple, Annu. Rev. Earth Planet. Sci. **21**, 333 (1993).
[34] R. M. Schmidt, *Proceedings of the 11th Lunar Planetary Science Conference* (Pergamon Press, Housten, Texas, 1980), pp. 2099–2128.
[35] S. Yamamoto, K. Wada, N. Okabe, and T. Matsui, Icarus **183**, 215 (2006).
[36] H. Mizutani, S. Kawakami, Y. Takagi, M. Kato, and M. Kumazawa, J. Geophys. Res. **88**, A835 (1983).
[37] M. J. Cintala, L. Berthoud, and F. Hörz, Meteorit. Planet. Sci. **34**, 605 (1999).
[38] H. Katsuragi, Phys. Rev. Lett. **104**, 218001 (2010).
[39] H. Katsuragi and D. J. Durian, Nat. Phys. **3**, 420 (2007).